

Article

A Challenging Tornado Forecast in Slovakia

Miroslav Šinger^{1,2,*}  and Tomáš Púčik³

¹ Department of Meteorology and Climatology, Faculty of Mathematics, Physics and Informatics, Comenius University, 84248 Bratislava, Slovakia

² Department of Weather Forecasting and Warnings, Slovak Hydrometeorological Institute, 83315 Bratislava, Slovakia

³ European Severe Storms Laboratory, 2700 Wiener Neustadt, Austria; tomas.pucik@essl.org

* Correspondence: miroslav.singer@shmu.sk

Received: 24 June 2020; Accepted: 31 July 2020; Published: 4 August 2020



Abstract: An F1 tornado hit the village of Lekárovce in eastern Slovakia on the afternoon of 3 October 2018. The tornado, which occurred outside the main convective season in Slovakia, was not anticipated by the meteorologists of the Slovak Hydrometeorological Institute. The models available to the forecasters simulated an environment of marginal convective available potential energy (CAPE) and weakening vertical wind shear. This paper addresses forecasting challenges associated with events related to a tornado threat. To investigate conditions before tornado formation, observational datasets, including sounding, and vertical-azimuth display (VAD) data from a radar station and surface stations were used. Hodographs based on observational data and a higher-resolution run of the limited-area model showed stronger lower tropospheric shear than was formerly anticipated over the area of interest. The higher-resolution model was able to better represent the modification of the lower tropospheric flow by a mountain chain, which was crucial to maintaining the strong lower tropospheric shear in the early afternoon hours before the tornado's occurrence. We discuss the importance of using both observational datasets and higher-resolution modeling in the simulation of lower tropospheric wind profiles, which affect the lower tropospheric storm relative helicity as one of the key ingredients in mesocyclonic tornadogenesis.

Keywords: tornado forecasting; supercell; vertical wind shear; storm relative helicity; streamwise vorticity; high-resolution NWP modeling

1. Introduction

Tornado forecasting has its roots in 1948, when Fawbush and Miller issued the first tornado forecast for Tinker Airbase in Oklahoma, United States. Since then, the science of tornado forecasting has advanced considerably, as documented by Brooks et al. (2019) [1]. Currently, tornadoes are forecast using the knowledge of the conditions, or so-called ingredients, required for their formation. Ingredient-based methodology is also used for forecasting of deep moist convection in general. Sufficient lower tropospheric moisture, conditionally unstable stratification, and a lift mechanism are required to form a convective storm [2,3].

In order to develop rotation in a storm (supercell), the presence of strong vertical wind shear in the deep layer of the troposphere is needed. The importance of vertical wind shear for mesocyclogenesis has been understood for decades, and it has been demonstrated both using environmental observations made in proximity to supercells [4,5] and through idealized numerical simulations [6]. A measure of the degree of streamwise vorticity in the inflow to the thunderstorm, storm relative helicity [7], is also used as a supercell predictor [8].

However, the majority of supercells never produce any tornadoes [9]. Scientists have used field experiments to gather more information on the differences between tornadic and nontornadic

supercells [10]. Together with idealized numerical simulations [11], these field experiments showed that tornadogenesis requires the presence of strong vertical wind shear near the ground, and downdraft air that is not too negatively buoyant. Stronger shear near the ground is associated with enhanced dynamic vorticity stretching, but also with stronger inflow that maintains a small horizontal distance between the parent mesocyclone and the vorticity maximum on the ground [12]. A downdraft that is too negatively buoyant cannot be vertically stretched, and may displace low-level circulation away from the mesocyclone [13]. For these reasons, measurements of storm relative helicity or bulk shear in the lowest 1 km, combined with the height of lifted condensation level, have been used to forecast significant tornadoes [5,14,15]. In Europe, bulk shear in the lowest 3 km was found to be a better discriminator between environments supporting no and significant tornadoes [16,17].

Further studies revealed that the degree of streamwise vorticity in the hundreds of meters above the ground that discriminates best between tornadic and nontornadic supercells [18,19]. Using numerical simulations of storms initiated with the composite sounding of tornadic and nontornadic supercells collected during the VORTEX 2 field project, Coffey et al. (2017) [20] and Coffey and Parker (2018) [21] showed that the degree of streamwise vorticity in the lowest few hundred meters determines whether a low-level mesocyclone can provide enough dynamical stretching of vertical vorticity to achieve tornadogenesis. Updating the composite parameters used to forecast tornadoes using this knowledge has led to improvements in the discrimination of nontornadic and tornadic environments [22].

Increasing the horizontal resolution of local-area models has allowed some of the characteristics of convective storms, such as updraft helicity [23] or vertically integrated graupel content within the updraft, to be explicitly simulated [24]. Increasing resolution has also led to increased performance of convective-wind-gust forecasts [25], and convection-allowing models (CAMs) have produced some very successful forecasts of severe-wind-gust-producing bow echoes, as demonstrated by Weisman et al. (2013) [26]. Updraft helicity was found to be a good discriminator of nonsevere and severe storms [27] and a good predictor of tornado-track length [28,29]. However, Clark et al. (2012) [28] also noted that the performance depended on the background environment, and that updraft-helicity tracks were better indicators of tornado activity in environments that were clearly favorable to tornadogenesis. Indeed, combining the explicit simulation of convective-cell characteristics with the background environment yielded the best tornado-forecasting performance [30–32]. While many of the aforementioned studies looked at mostly high convective available potential energy (CAPE) and strongly sheared environments, Lawson (2019) [33] noted that explicit simulations of storm intensity exhibit large uncertainty in environments with low CAPE but strong vertical wind shear. This type of environment, as in the present case, is notorious for both lower tornado prediction and warning performance across the U.S. [34,35].

While considerable research and effort have been focused on tornado forecasting and damage documentation in the U.S., tornado forecasting and post-storm field surveys are typically not a part of a meteorologist's job in Slovakia. To date, the climatology of tornadoes over Slovakia has not yet been reported. Only five cases were recorded in the past 10 years (2010–2020), according to the European Severe Weather Database [36]. Supercells, which are responsible for most strong and violent tornadoes [37], occasionally occur in Slovakia with an average of 3–4 supercell days detected in 2000–2012 [38]. Recently, the construction of new, higher-quality radars has led to higher rates of supercell detection. For example, in 2017, 25 days with supercells with over 80 individual supercells were recorded [38], but no tornadoes were reported. Thus, the percentage of supercells that succeed at tornadogenesis is likely much lower than that in the U.S.

This paper describes the case of a tornado on 3 October 2018, which hit the village of Lekárovice in eastern Slovakia. The event was observed by numerous eyewitnesses and became the first mesocyclonic tornado in Slovakia that was photographically documented. The tornado was rated F1 on the basis of the damage survey done by a local storm spotter [39]. It was not anticipated by the forecasters of Slovak Hydrometeorological Institute. It occurred outside the standard convective season in Slovakia,

which runs from May to September, and the numerical models used by forecasters did not simulate the presence of strong shear in the lowest 1 km of the troposphere.

This paper had three goals:

1. Reconstruct the environment of the parent storm using observational data and compare it to the Aire Limitée Adaptation Dynamique Développement InterNational (ALADIN) model made available to forecasters several hours before the event.
2. Use a higher-resolution run of the ALADIN system to simulate the preconvective environment.
3. Find out whether observational data or the high-resolution run of the model would help forecasters to recognize favorable conditions for tornadogenesis using the most recent knowledge on the topic.

2. Methodology

To investigate synoptic-scale weather conditions, we used the European Center for Medium-Range Weather Forecast (ECMWF) operational global hydrostatic numerical weather prediction (NWP) model with a horizontal grid spacing of 0.1° . For smaller scales, we used local-area NWP models: operational model ALADIN of the Slovenský Hydrometeorologický Ústav (SHMU) (OPM) and experimental local-area model ALADIN/ELAM (ELAM). OPM is a hydrostatic model with convection parametrization, and ELAM is a nonhydrostatic high-resolution model computed as dynamic downscaling from OPM on smaller domains. The 3MT scheme [40] was used for the parameterization of deep convection in the cases of both OPM and ELAM. This scheme proved to work well with partially resolved deep convection in 1–2.5 km grid spacing [41]. We did not experiment with changes in any parameterization schemes when switching between OPM and ELAM. ELAM has higher horizontal and vertical resolution, which results in better topographical descriptions. Both models were utilized with high-performance computers (HPC) at the Slovak Hydrometeorological Institute [42]. The technical settings of the NWP models are summarized in the Table 1, and their domains are shown in Figure 1a. More detailed descriptions can be found in Termonia et al. (2018) [43]. Forecasters did not have the ELAM output available.

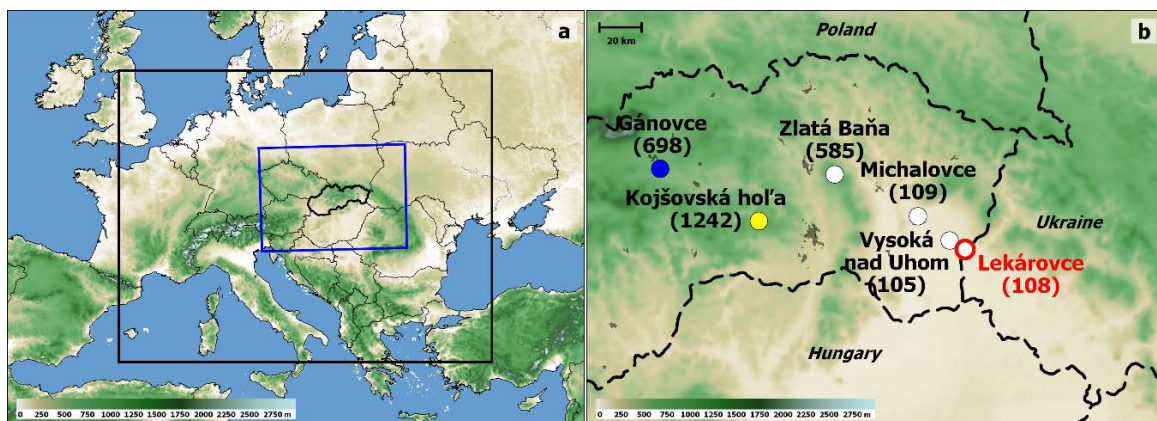


Figure 1. (a) Model domains in the study. OPM domain outlined by black rectangle, ELAM domain outlined by blue rectangle. Real topography shown as background. (b) Map zoomed on eastern Slovakia, showing locations discussed in the text. Country names shown in italics; tornado location highlighted in red. Other sites represent weather stations; altitude given in m a.s.l. in brackets. Blue circle: Gánovce sounding station; yellow circle: location of Kojšovská hoľa radar. Northeast of Michalovce is the Vihorlat mountain chain, south of the Vihorlat mountains is Východoslovenská nížina lowland. Black areas: locations of larger towns in Slovakia.

Table 1. Description of numerical weather prediction (NWP) operational model Aire Limitée Adaptation Dynamique Développement InterNational (ALADIN) of the Slovenský Hydrometeorologický Ústav (SHMU) (OPM) and ALADIN Experimental Local-Area Model (ELAM).

Description	ALADIN/SHMU (OPM)	ALADIN/ELAM (ELAM)
Horizontal resolution	4.5 km	1 km
Number of grid points	625 × 576	1000 × 720
Spectral resolution	312 × 278 (linear truncation)	499 × 359 (linear truncation)
Number of vertical levels	63	73
Dynamics	Hydrostatic	Nonhydrostatic
Physics	ALARO-1vB	ALARO-1vB
Microphysics	Lopez [44]	Lopez [44]
Deep convection	3MT [40]	3MT [40]
Time step	180 s	60 s
Coupling model	ARPEGE	ALADIN/SHMU
Coupling frequency	3 h	1 h
Assimilation	Upper-air spectral blending with CANARI surface assimilation	Dynamical downscaling
Run	3 October 2018, 06:00 Coordinated Universal Time (UTC)	3 October 2018, 06:00 UTC
Forecast range	72 h	12 h

In order to reconstruct the hodograph for the time of tornadogenesis, we used observational data from synoptic stations, the radar station from Kojšovská hoľa mountain [45], and the sounding station from Gánovce (Figure 1b). Local solar time in eastern Slovakia is approximately +1 h compared to Coordinated Universal Time (UTC).

3. Results

3.1. Prestorm Environment According to Numerical Models Available to Forecasters

Environmental conditions are discussed on the basis of NWP model data available to the morning shift at the local hydrometeorological service, namely, the 00 UTC run of ECMWF and the 06 UTC run of the local-area NWP OPM.

Slovakia was on the southeastern edge of a low-pressure system (Figure 2) that moved from the Baltic Sea towards Belarus. In the prevailing northwesterly flow, polar maritime airmass was advected over central Europe. The airmass was characterized by a lapse rate of 6 to 7 °C·km⁻¹ and surface dew point of 7–10 °C (Figure 3a). This allowed for marginal CAPE values of up to 500 J·kg⁻¹ (Figure 3b) and a chance for deep moist convection to develop, as the lift was provided by a convergence zone in a surface-pressure trough. The best overlap of conditionally unstable lapse rates and sufficient lower tropospheric moisture, along with the highest CAPE values, was simulated in the afternoon hours over eastern Slovakia. Vertical wind shear decreased over the morning and into the afternoon hours, and 500 hPa surface-layer bulk values (deep-layer shear, DLS) dropped from 40 to 20 m·s⁻¹, which would still be sufficient for well-organized convection, including supercells [5].

Forecast soundings over eastern Slovakia at 10:00 and 12:00 UTC on Figure 4 showed that the steepest lapse rates were in the lowest 3 km, strengthening at noon with an equilibrium level of 5.5 km, suggesting low-topped convection. While DLS remained strong throughout the day, storm relative helicity in the 0–1 km layer decreased from 60–100 m²·s⁻² in the morning to 10–50 m²·s⁻² in this timeframe. The decrease was due to the veering of surface-wind change from the southern to the western direction (Figure 5). This would suggest that the environment had become less conducive to tornadogenesis [46]. Meteorologists considered the overall severe convective storm threat to be low, given the marginal values of CAPE and only weak vertical wind shear in the lower troposphere.

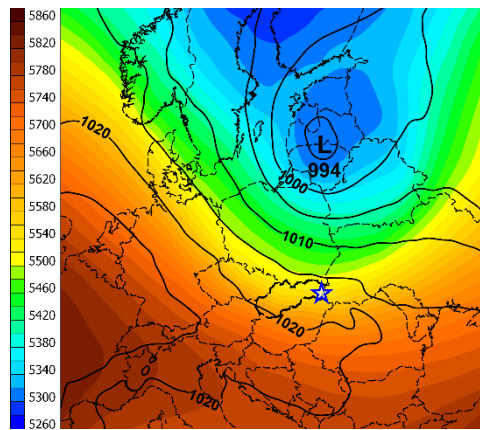


Figure 2. European Center for Medium-Range Weather Forecast (ECMWF) forecast on 3 October 2018 00:00 UTC of 12:00 UTC mean sea-level pressure (black isolines) (hPa) and geopotential height of 500 hPa (color scale) (gpm). Tornado location highlighted by blue star.

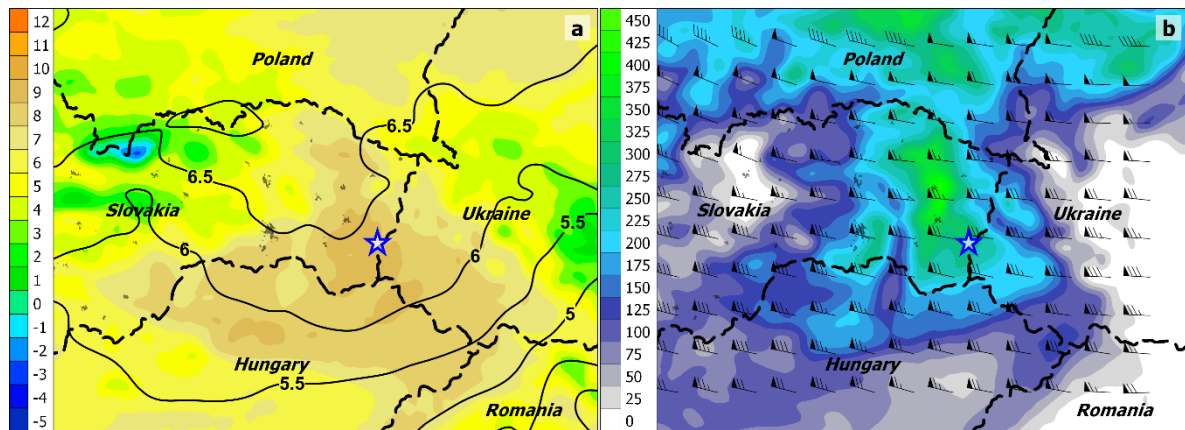


Figure 3. (a) NWP OPM forecast on 3 October 2018 06:00 UTC of 12:00 UTC. (a) Average lapse rate in 900–600 hPa layer (black isolines) ($^{\circ}\text{C}\cdot\text{km}^{-1}$) and dew-point temperature at 2 m (color scale) ($^{\circ}\text{C}$); (b) surface-based convective available potential energy (CAPE; color scale) ($\text{J}\cdot\text{kg}^{-1}$) and deep-layer shear (DLS; wind barbs: full barb, $5\text{ m}\cdot\text{s}^{-1}$; half barb, $2.5\text{ m}\cdot\text{s}^{-1}$; flag, $25\text{ m}\cdot\text{s}^{-1}$). Country names shown in italics; tornado location highlighted by blue star.

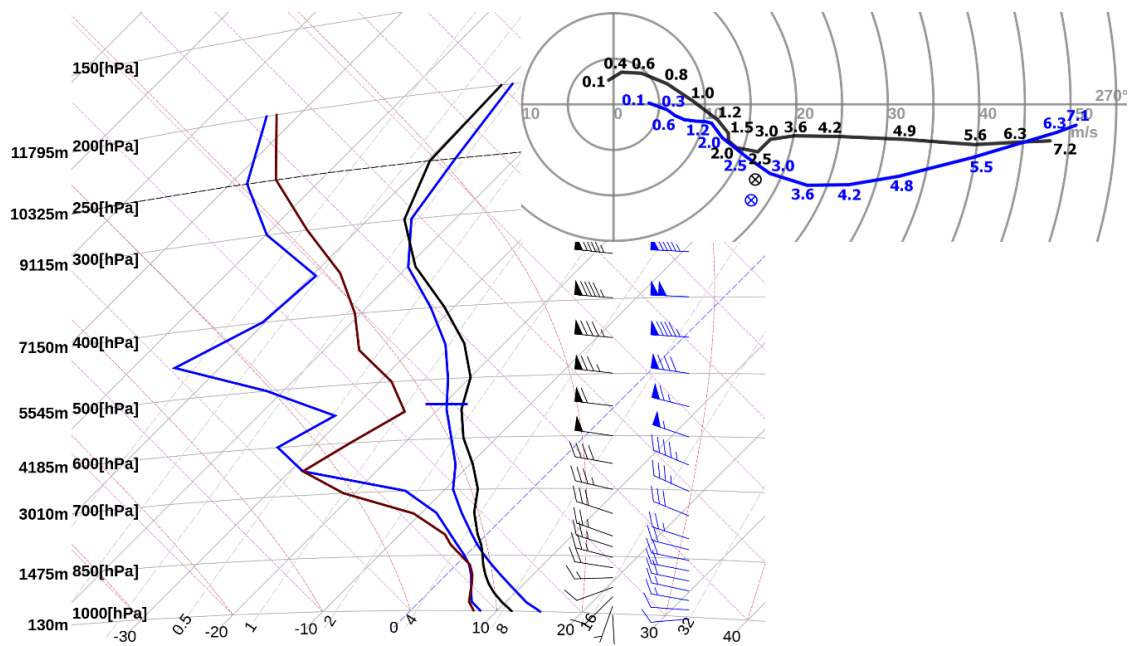


Figure 4. NWP OPM forecast tephigrams, vertical wind profiles, and hodographs on 3 October 2018 06:00 UTC with plotted storm motion vectors (crossed circles) and numbers corresponding to heights in km valid for southeastern Slovakia; NWP OPM at 10:00 UTC (black), and 12:00 UTC (blue). Equilibrium level calculated for 12:00 UTC denoted by horizontal blue line; location of forecast tephigrams denoted in Figure 5.

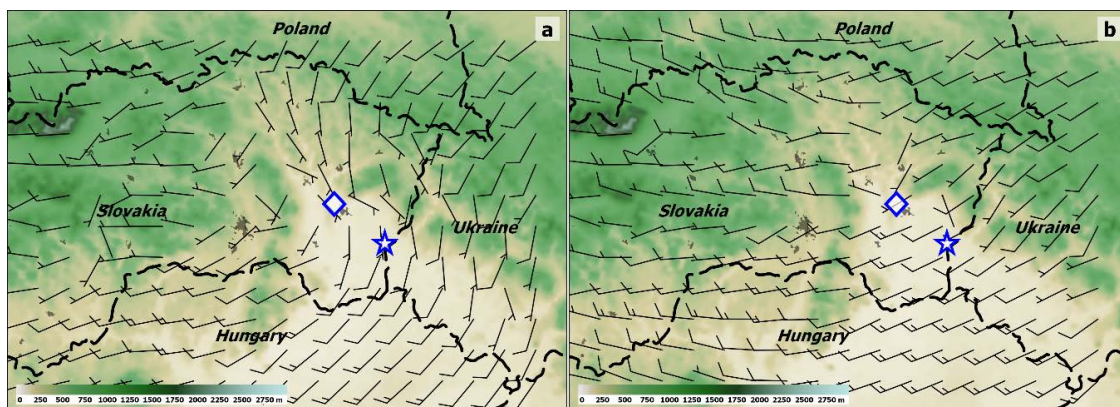


Figure 5. NWP OPM forecast of surface winds on 3 October 2018 06:00 UTC ($\text{m}\cdot\text{s}^{-1}$) over eastern Slovakia at (a) 08:00 and (b) 12:00 UTC. Real topography shown as background; polygons: locations of larger towns in Slovakia. Country names shown in italics; tornado location highlighted by blue star; tephigram location from Figure 4 highlighted by blue rhombus.

3.2. Observational Data

Different observational datasets that could be used to infer the degree of vertical wind shear were available to the forecasters before the time of the tornado. These included radar data, surface-wind observations, and radiosonde data from the Gánovce station.

Before the tornado, a parent storm evolved from a small cluster of showers that formed shortly after 12 UTC. The storm attained supercell characteristics at 13:40 UTC, marked by the presence of a mesocyclone, deviant movement to the right, and the presence of both a bounded weak echo region (BWER) and a hook echo (Figure 6). Supercell characteristics persisted till 15:00 UTC. The tornado occurred at 14:30 UTC in the Lekárovce village on the Slovak–Ukrainian border and lasted for around

10 min [38]. As the storm strengthened after 13:00 UTC, the present paper focuses on the available observations from around this period.

Surface observations available from the early afternoon hours showed a discrepancy between model simulation and reality. While the model predicted a westerly wind over southeastern Slovakia and western Ukraine at 12:00 UTC (Figure 5b), surface observations revealed the presence of an easterly flow, reaching up to $5 \text{ m}\cdot\text{s}^{-1}$ ahead of a shallow trough (Figures 7 and 8). Furthermore, a southerly wind, instead of a westerly wind as simulated by the models, was observed over the northern part of eastern Slovakia. On the basis of this information, a forecaster could have expected stronger vertical wind shear than what was forecast, given the easterly flow veering to strong westerlies in the mid-to-upper troposphere.

In order to obtain information about the wind above the surface and to recreate a hodograph of the vertical wind profile before the tornado, we also investigated sounding observations from Ganovce at 12:00 UTC (Figure 9), and the vertical-azimuth display (VAD) from the radar station located at Kojšovská hoľa (not shown).

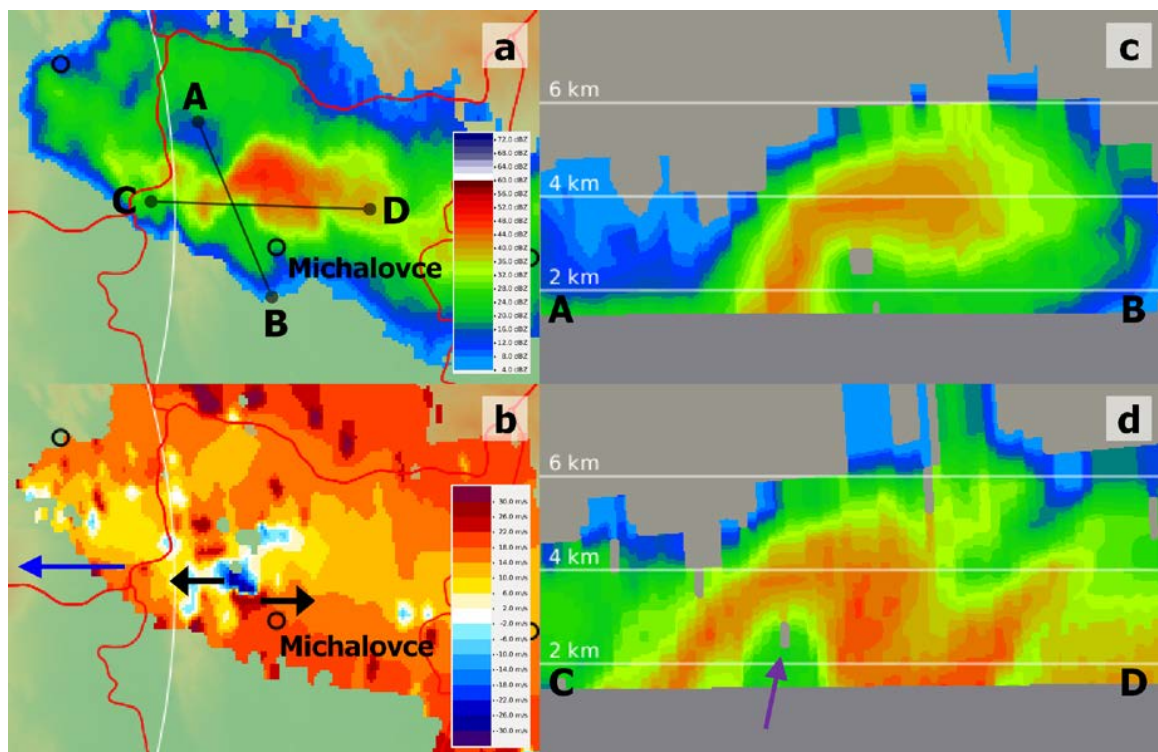


Figure 6. Radar supercell features near Michalovce on 3 October 2018 13:50 UTC, observed from the radar station Kojšovská hoľa, (a) CAPPI 2 km (dBZ). (b) Radial velocity at 1.5° elevation ($\text{m}\cdot\text{s}^{-1}$); blue arrow points towards the radar location, black arrows indicate mesocyclone. (c,d) Vertical cross-sections (dBZ), purple arrow points to bounded weak echo region (BWER). Cross-section locations indicated by AB and CD segments.

Radiosounding, like the model forecast (Figure 4), measured a strong westerly flow, increasing to $50 \text{ m}\cdot\text{s}^{-1}$ at 400 hPa. While the wind at the mid-to-upper troposphere may be representative of the environment in which the tornado occurred, about 120 km southeast of the sounding site, its representativeness in the lower altitudes is questionable. First, sounding was launched in the rear side of the trough, with surface flow already having veered to being westerly forecast (Figure 4). Second, the site is located at a higher altitude (706 m) than the tornado location (108 m). Therefore, a wind profile from the lower levels from sounding was not useful for the investigation of the vertical wind profile in the tornado location.

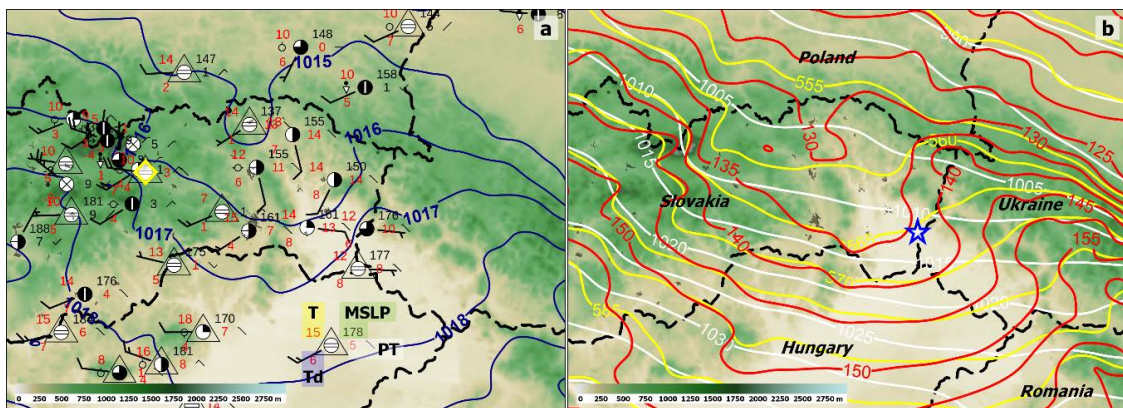


Figure 7. (a) Surface weather-station observations on 3 October 2018 12:00 UTC based on synoptic reports and analysis of mean sea-level pressure (hPa). Surface-station plots: T, air temperature (°C); Td, dew-point temperature (°C); MSLP, mean sea-level pressure (hPa); PT, 3-h pressure tendency (10^{-1} hPa); cloudiness represented by circles, and wind by wind barbs. Triangles, automatic weather stations; yellow rhombus, highlighted sounding location from Figure 9. (b) NWP OPM analysis of geopotential heights on 3 October 2018 12:00 UTC at 1000 (red), 950 (yellow), and 900 hPa (white) (gpm). Country names shown in italics; tornado location highlighted by blue star.

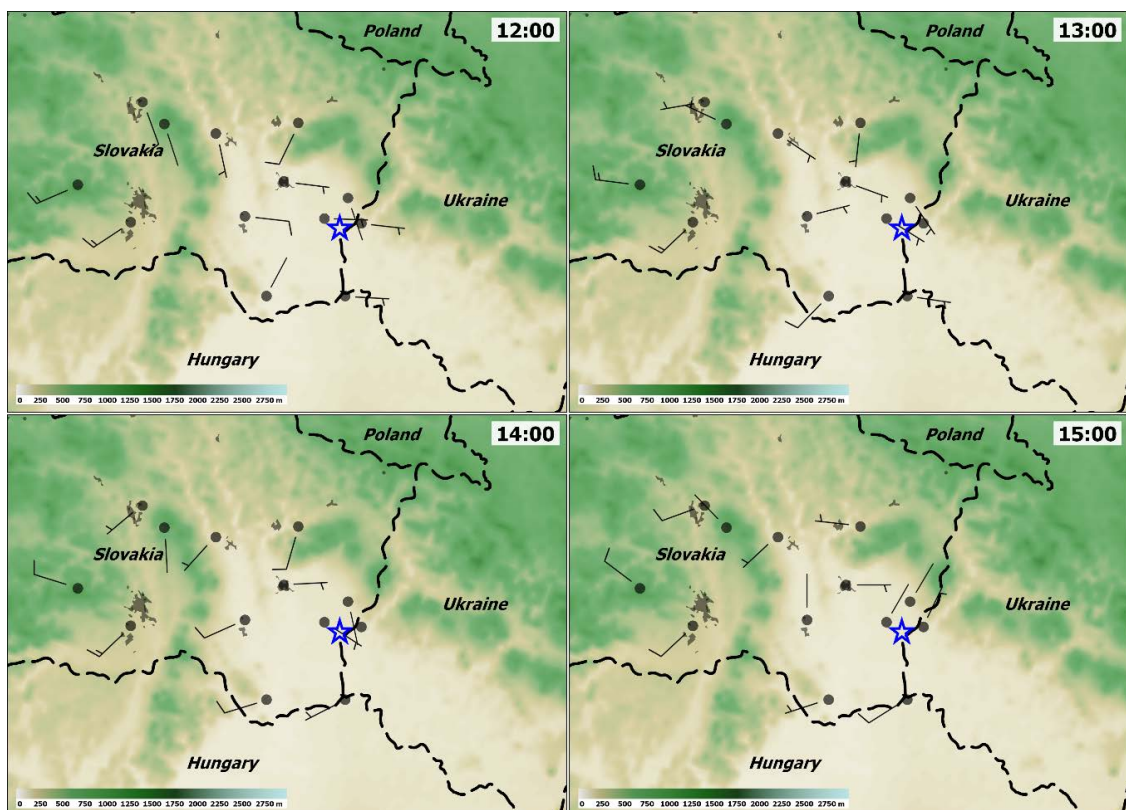


Figure 8. Surface-wind observations on 3 October 2018, 12:00–1500 UTC based on synoptic reports. Country names shown in italics; tornado location highlighted by blue star.

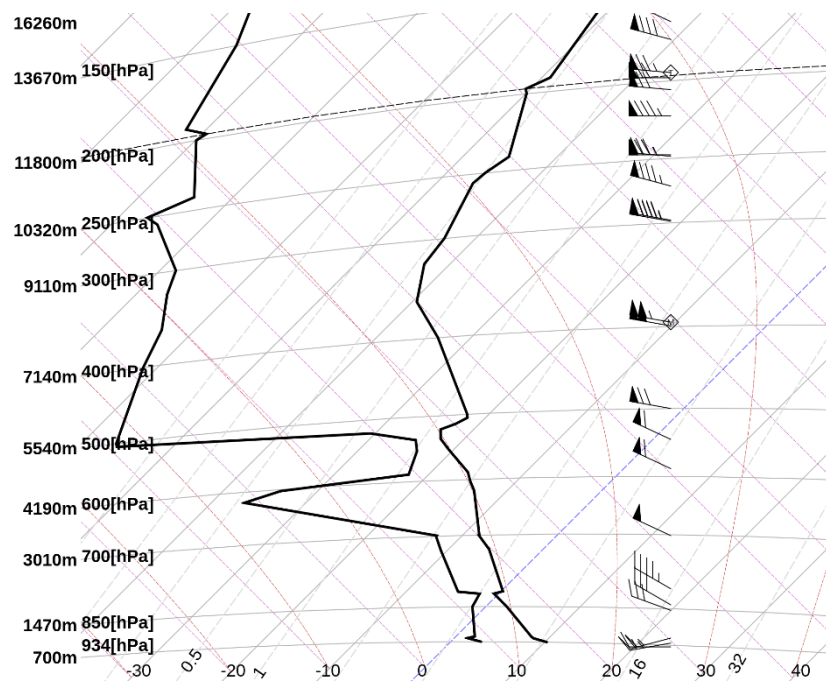


Figure 9. Gánovce sounding measured on 3 October 2018 12:00 UTC.

VAD measurements were available from the Kojšovská hoľa radar site, starting at an altitude of 1.2 km a.s.l. and about 85 km west–northwest of the tornado location, thus being closer than the sounding measurement. The only complete measurement for the altitude of 1.2 to 4 km was available at 12:50 UTC, with a marked increase in westerly wind, though the increase was not as significant as in the case of the Ganovce sounding station. Data above 4 km were not available from VAD. To decide whether to use sounding or VAD to represent the vertical wind profile between 1.2 and 4 km, we compared the right-moving storm-motion vector calculation using both datasets with the real observed storm motion (Figure 10). To consider the low-topped nature of the storm on the basis of the forecast (Figure 4) and observed height (Figure 6c,d and Figure 9) of the equilibrium level, which was close to 5.5 km, we used a 0–4 km mean wind and 0–4 km shear vector when applying the Bunkers et al. (2000) method [47]. Using VAD instead of the sounding data in the aforementioned layer yielded a more precise calculation of a storm-motion vector (Figure 10). VAD measurements were also closer to the tornado location than the sounding. Thus, we considered the VAD to be more representative of the wind profile over the tornado location than sounding. Sounding data were used to infer the vertical wind profile for the altitude above 4 km, where VAD data were not available.

Using either sounding or VAD still left us without any knowledge regarding the wind profile in the crucial layer of the bottom 1 km. To fill this gap, we used the measurements from the stations of Michalovce, Vysoká and Uhom, and Zlatá Baňa and Kojšovská hoľa (their locations are shown in Figure 1b), which represented altitudes from 100 to 1200 m. These observations were used to represent the wind field at various heights as if these wind observations were taken over the tornado location. In order to reconstruct the conditions that would be the most conducive to tornadogenesis, we took into consideration the maximal observed wind speeds within 1 h of the change in wind direction associated with the passage of the surface trough. Thus, a 13:27 measurement was taken from Michalovce, 14:14 from Vysoká and Uhom, and 11:22 UTC from Zlatá Baňa. The VAD profile from Kojšovská hoľa was considered only for the time at which a complete wind profile was available to 4 km, which was at 12:50 UTC. While this may be the most accurate way to infer the wind profile on the basis of the limited availability of observational datasets, it is still likely an imperfect representation of the true wind profile near the tornado location. One of the primary limitations is the effect of friction

on wind in the surface stations that were used to represent the wind vector that would be hundreds of meters above ground at the tornado location.

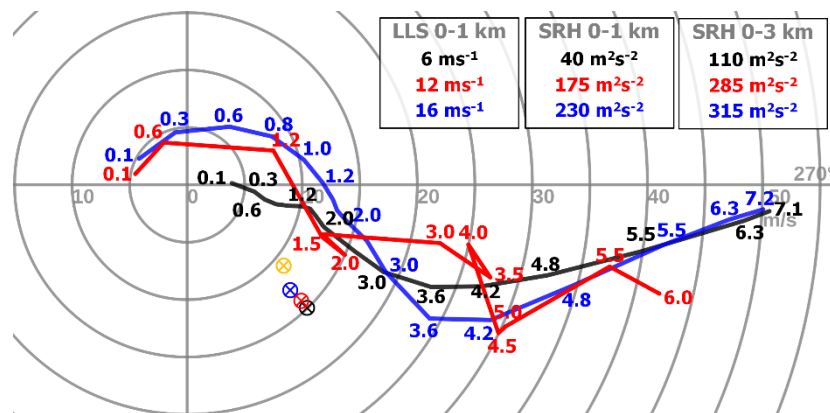


Figure 10. Hodographs representing the Michalovce area before tornadogenesis based on observations from weather stations, Gánovce sounding, and vertical-azimuth display (VAD) Kojšovská hoľa (red) simulation of 3 October 2018, 06:00 UTC NWP OPM run (black), and 3 October 2018, 06:00 UTC ELAM run (blue). Crossed circles: storm-motion vectors (SMVs); orange: real SMV derived from track of weak-echo region in radar data. Other SMVs computed by Bunkers method on basis of wind data in 0–4 km layer and for wind profiles from respective datasets. Values of observed simulated low-level wind shear (LLS) and storm relative helicity (SRH) in 0–1 and 0–3 km layers shown in top-right corner.

Because of the distances between individual weather stations to the tornado site, and the fact that they represent the wind field under the influence of friction, a reconstructed wind profile offers only a rough estimation of reality. Nevertheless, comparing the forecast hodograph using OPM to the reconstructed hodograph clearly showed that the model underestimated the lower tropospheric wind shear (Figure 10). The forecast wind profile would result in about $6 \text{ m}\cdot\text{s}^{-1}$ of bulk shear and $40 \text{ m}^2\text{s}^{-2}$ of storm relative helicity (SRH) in the 0–1 km layer, compared to $12 \text{ m}\cdot\text{s}^{-1}$ and $175 \text{ m}^2\text{s}^{-2}$ in the reconstructed profile. Shear in the 0–3 km layer was also substantially stronger in the reconstructed wind profile, with SRH reaching $285 \text{ m}^2\text{s}^{-2}$, in contrast to $110 \text{ m}^2\text{s}^{-2}$ based on the forecast profile. Such values have been associated with tornadoes both in the U.S. [5,46,48] and Europe [16,17,49]. “Kink” in the lowest 500 m of the reconstructed hodograph also suggested almost purely streamwise vorticity in the inflow to the storm in that layer, a condition that was deemed favorable for tornadogenesis by Coffey et al. (2017) [20]. Using an observational dataset in lieu of model simulation in this case would allow forecasters to recognize a higher-than-expected tornado threat.

3.3. High-Resolution Experimental Local-Area Model (ELAM)

A nonhydrostatic, 1 km grid-spaced run of an ELAM-simulated environment was considerably more conducive to tornadogenesis than the OPM 4.5 km run. The spatial distribution of SRH 0–1 km (Figure 11) showed local maxima in the vicinity of the town of Michalovce with values up to $230 \text{ m}^2\text{s}^{-2}$, compared to $10\text{--}40 \text{ m}^2\text{s}^{-2}$ from the OPM run and $175 \text{ m}^2\text{s}^{-2}$ from the reconstructed hodograph (Figure 10). The 0–1 km bulk shear was also much stronger in the ELAM run ($16 \text{ m}\cdot\text{s}^{-1}$ compared to $6 \text{ m}\cdot\text{s}^{-1}$ in the OPM run). However, the simulated SRH maximum was not precisely collocated with the town of Lekárovce, where the ELAM simulated around $80 \text{ m}^2\text{s}^{-2}$ compared to $50 \text{ m}^2\text{s}^{-2}$ in OPM. Differences in the SRH and 0–1 bulk shear between OPM and ELAM runs were due to the treatment of the lower tropospheric wind field. OPM simulated a straight hodograph with a westerly wind at the surface, veering to a northwesterly direction with height. ELAM simulated a curved hodograph with east–southeasterly flow at the surface, veering through southerly directions to a west–southwesterly flow in the bottom 1 km.

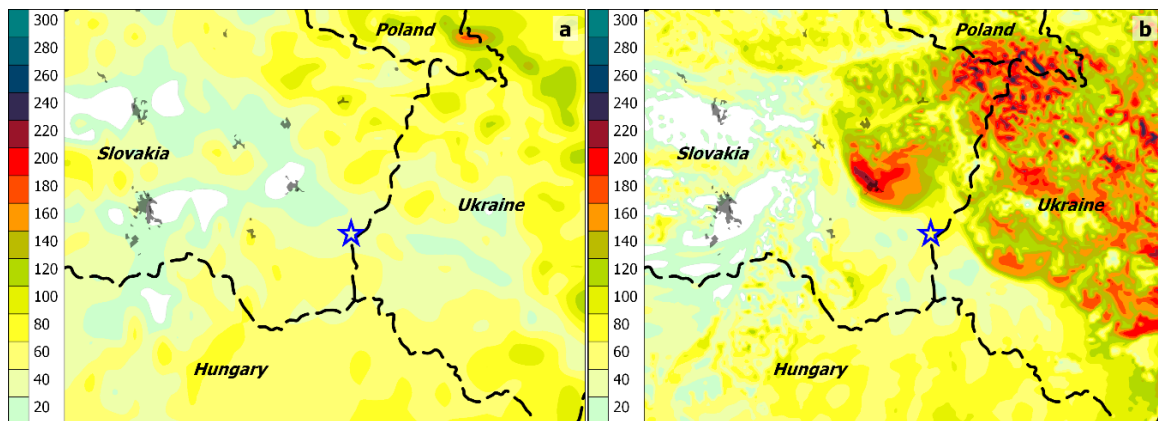


Figure 11. Forecast on 3 October 2018 06:00 UTC of 12:00 UTC storm relative helicity in 0–1 km layer (m^2s^{-2}) over eastern Slovakia based on (a) NWP OPM and (b) ELAM. Country names shown in italics; tornado location highlighted by blue star.

The reconstructed hodograph resembled the one simulated by ELAM in the bottom 500 m, but did not show southerly wind directions between 500 m and 1.2 km (Figure 10). Instead, the wind immediately turned to the west–southwest. This may have been because there was a large gap in observational data between 585 m and 1.2 km. It is likely that if such data had been available, the reconstructed hodograph would have involved more curvature and a higher SRH. Furthermore, weather-station data were representative of wind 10 m above the ground, strongly affected by surface friction. In reality, altitudes of 585 m and 1.2 km would be hundreds of meters above ground at the tornado location, which was at an altitude of 108 m a.s.l.

Differences in the wind field in the lower troposphere between OPM and ELAM forecasts can be attributed to differences in the simulation of the surface trough, and its shape and movement (Figure 12). ELAM simulated the slower movement of the surface trough, as it was located more to the west at both 11:00 and 14:00 UTC than in the OPM simulation. At 14:00 UTC, Lekárovice was located north of the small-scale low in the ELAM run, yielding a southeasterly flow, but west of the small-scale low in the OPM run, yielding a westerly flow at the surface. Besides the difference in the trough movement speed, its shape was also distinctive. Smaller-scale troughs and ridges were better identifiable in the ELAM run. These features were also identifiable near the tornado location, with a trough over the lowland and a ridge over the Vihorlat mountain chain. OPM had already forecast a change in the surface-wind direction between 11:00 and 12:00 UTC, while ELAM predicted the change to happen between 13:00 and 14:00 UTC (Figure 13).

ELAM's predicted change of wind shift between 13:00 and 14:00 UTC was better than that of OPM, but also not completely accurate. Surface observations showed an easterly flow persisting till 15:00 UTC over the tornado area and covering a larger area (Figure 8) than that simulated by the model. Directly over Lekárovice, ELAM simulated a southwesterly surface flow, in contrast to the easterly flow in the surface observations. Thus, it is likely that the SRH bullseye, simulated only to the immediate south of Vihorlat, expanded further to the southeast, covering Lekárovice as well. Nevertheless, the ELAM prediction better represented an environment supportive of tornadoes compared to that of OPM. In the case of operational usage, forecasters could be more aware of the significant lower tropospheric shear over the Slovakia/Ukraine border.

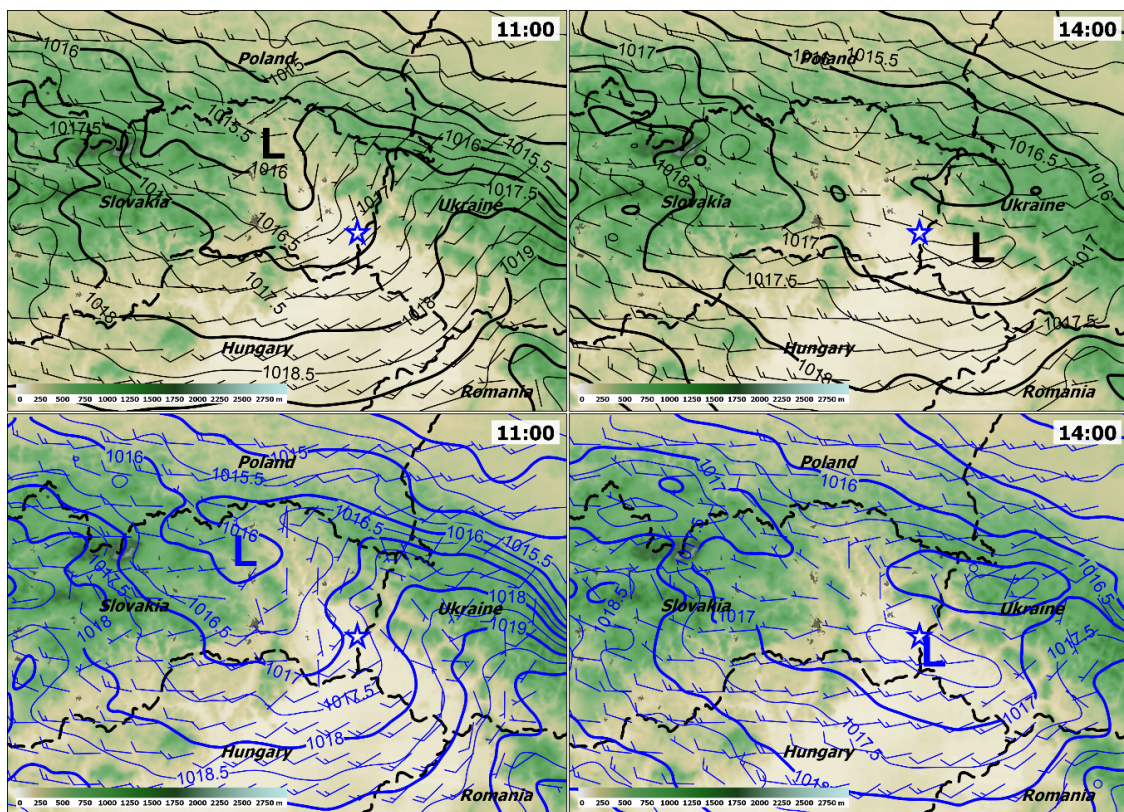


Figure 12. Model-run forecast on 3 October 2018 06:00 UTC for 11:00 and 14:00 UTC mean sea-level pressure and surface winds over eastern Slovakia based on NWP OPM (black) and ELAM (blue). Center of shallow trough/low marked by “L”. Country names shown in italics. Tornado occurred at 14:30 UTC; its location is highlighted by blue star.

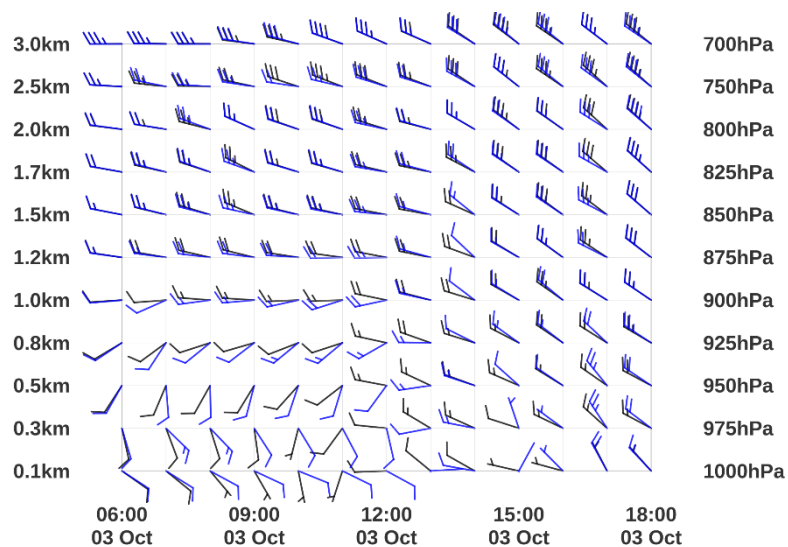


Figure 13. Forecast on 3 October 2018 06:00 UTC of temporal evolution of winds in a 0–3 km layer near Michalovce (same point as Figure 4) based on OPM (black wind barbs) and ELAM (blue wind barbs).

4. Discussion and Conclusions

On 10 October 2018, a tornado hit Lekárovce village in eastern Slovakia, causing F1 damage to numerous structures. While tornadoes are rare in Slovakia, they do occur, as demonstrated by this and some previous cases [36,50–53]. Therefore, operational forecasters need to be able to identify

environments conducive to tornadogenesis using both NWP models and observational datasets. This paper concentrated on discussing the possibility of identifying such an environment for the Lekárovice case using the NWP models and observational datasets available to forecasters at the time of the tornado, as well as using a higher-resolution run of the NWP model.

The operational NWP ALADIN/SHMU model forecast a collocation of favorable ingredients for deep-moist convection in the afternoon hours over eastern Slovakia at the time, when the degree of lower tropospheric shear was supposed to markedly decrease since the morning hours. However, the reconstructed hodograph from the available observational data showed stronger lower tropospheric shear, approaching magnitudes commonly found with tornadoes in the literature. Thus, it is crucial for the forecasters to utilize these observational datasets in conjunction with NWP models in order to identify tornado threats associated with storms forming over eastern Slovakia.

Experimental NWP ALADIN/ELAM yielded even stronger vertical wind shear than from the reconstructed hodograph in the lower troposphere over the area of interest. The main difference with respect to the OPM was the slower eastward progression of the surface trough through eastern Slovakia. Lekárovice remained on the forward flank of the trough, with southerly–easterly lower tropospheric flow until the early afternoon hours, when the storms formed and utilized the highly sheared environment. Furthermore, ELAM was able to better resolve smaller-scale troughs and ridges. The easterly direction of the surface wind can be explained by a ridge to the north and a trough to the south of the Vihorlat mountain chain that were not present in the OPM run. The easterly wind's changing to southerly and then northwesterly with height yielded a long and curved hodograph with large amounts of streamwise vorticity in the ELAM run, in contrast to the shorter and straight hodograph with pure crosswise vorticity in the OPM run. This could have been caused by orography differences between the 4.5 km OPM and 1 km ELAM (Figure 14). Using both the higher-resolution model and the observational data would have provided forecasters with enough clues regarding the environment that was prone to tornadoes on the given day. The importance of using observational datasets and high-resolution runs of NWP models for addressing flow modifications and subsequent shear enhancement by local topography was realized in other works, such as Bosart et al. (2006), Peyraud (2013), Tang et al. (2016), Lyza and Knupp (2018), and Lyza et al. (2020) [54–58]. Pilgaj et al. (2019) [59] reported overall improvement in the model forecast of tornadic supercells over Poland with both increasing horizontal resolution and the assimilation of surface observations and sounding data.

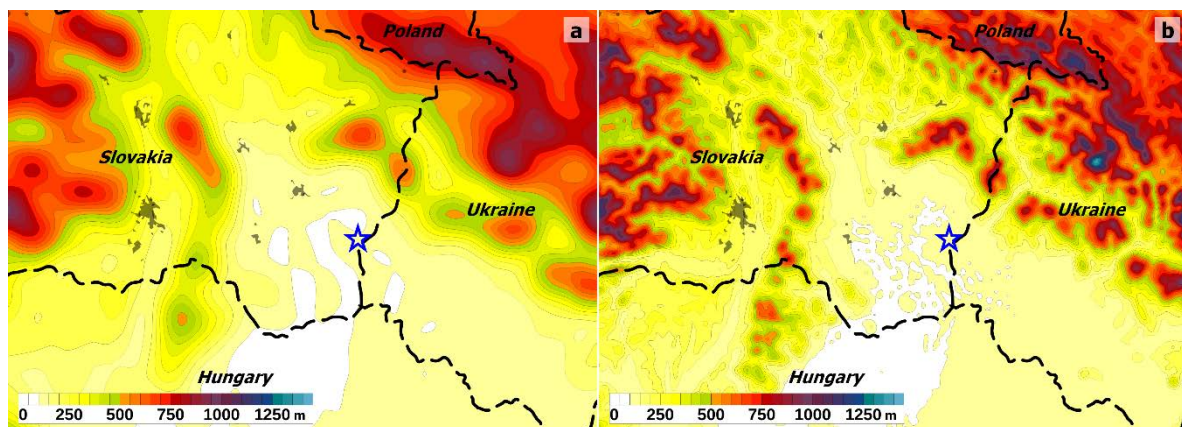


Figure 14. Model topography of NWP (a) OPM with grid spacing of 4.5 km and (b) ELAM with grid spacing of 1 km. Country names shown in italics; tornado location highlighted by blue star.

Analysis of more cases of severe convection in the area is necessary to draw general conclusions on the influence of local orography. Nevertheless, this case demonstrated the need for higher-resolution modeling of lower tropospheric flow, and for attention to be paid to observational data in situations

where environments conducive to severe weather are confined to a rather small area and possibly influenced by topography.

In addition to the operational model discussed in the publication, a convection-allowing model was operationally implemented in the Slovak Hydrometeorological Institute with the same settings as were used for the ELAM (Table 1), but with grid spacing of 2 km. With the purchase of a new supercomputer, it is planned that the model resolution and the size of its forecast domain will be further increased.

Author Contributions: Conceptualization, M.Š. and T.P.; methodology, M.Š. and T.P.; software, M.Š.; validation, T.P.; investigation, M.Š. and T.P.; resources, M.Š.; data curation, M.Š.; writing—original-draft preparation, M.Š. and T.P.; writing—review and editing, T.P.; visualization, M.Š.; validation, M.Š. and T.P.; project administration, M.Š. All authors have read and agreed to the published version of the manuscript.

Funding: This research received no external funding.

Acknowledgments: We would like to thank to Department of Numerical Weather Prediction of the Slovak Hydrometeorological Institute for the co-ordination, setup, and advice with the NWP models, namely, M. Derková, A. Simon, and M. Dian. Additional thank to M. Gera from the Department of Meteorology and Climatology, Faculty of Mathematics, Physics, and Informatics, Comenius University. We would also like to thank the three anonymous reviewers for their time and constructive comments. This article was partly supported by the Grant Agencies of the Slovak Republic under project Vega No. 1/0940/17.

Conflicts of Interest: The authors declare no conflict of interest.

References

1. Brooks, H.E.; Doswell, C.A., III; Zhang, X.; Chernokulsky, A.A.; Tochimoto, E.; Hanstrum, B.; de Lima Nascimento, E.; Sills, D.M.; Antonescu, B.; Barrett, B. A century of progress in severe convective storm research and forecasting. *Meteorol. Monographs*. **2019**, *59*, 18.1–18.41. [\[CrossRef\]](#)
2. Johns, R.H.; Doswell, C.A., III. Severe local storms forecasting. *Weather Forecast.* **1992**, *7*, 588–612. [\[CrossRef\]](#)
3. Doswell, C.A., III; Brooks, H.E.; Maddox, R.A. Flash flood forecasting: An ingredients-based methodology. *Weather Forecast.* **1996**, *11*, 560–581. [\[CrossRef\]](#)
4. Rasmussen, E.N.; Blanchard, D.O. A baseline climatology of sounding-derived supercell and tornado forecast parameters. *Weather Forecast.* **1998**, *13*, 1148–1164. [\[CrossRef\]](#)
5. Thompson, R.L.; Edwards, R.; Hart, J.A.; Elmore, K.L.; Markowski, P. Close proximity soundings within supercell environments obtained from the rapid update cycle. *Weather Forecast.* **2003**, *18*, 1243–1261. [\[CrossRef\]](#)
6. Weisman, M.L.; Klemp, J.B. The dependence of numerically simulated convective storms on vertical wind shear and buoyancy. *Mon. Weather Rev.* **1982**, *110*, 504–520. [\[CrossRef\]](#)
7. Davies-Jones, R. Streamwise vorticity: The origin of updraft rotation in supercell storms. *J. Atmos. Sci.* **1984**, *41*, 2991–3006. [\[CrossRef\]](#)
8. Thompson, R.L.; Mead, C.M.; Edwards, R. Effective storm-relative helicity and bulk shear in supercell thunderstorm environments. *Weather Forecast.* **2007**, *22*, 102–115. [\[CrossRef\]](#)
9. Trapp, R.J.; Stumpf, G.J.; Manross, K.L. A reassessment of the percentage of tornadic mesocyclones. *Weather Forecast.* **2005**, *20*, 680–687. [\[CrossRef\]](#)
10. Markowski, P.M.; Straka, J.M.; Rasmussen, E.N. Direct surface thermodynamic observations within the rear-flank downdrafts of nontornadic and tornadic supercells. *Mon. Weather Rev.* **2002**, *130*, 1692–1721. [\[CrossRef\]](#)
11. Markowski, P.M.; Richardson, Y.P. The influence of environmental low-level shear and cold pools on tornadogenesis: Insights from idealized simulations. *J. Atmos. Sci.* **2014**, *71*, 243–275. [\[CrossRef\]](#)
12. Guarriello, F.; Nowotarski, C.J.; Epifanio, C.C. Effects of the low-level wind profile on outflow position and near-surface vertical vorticity in simulated supercell thunderstorms. *J. Atmos. Sci.* **2018**, *75*, 731–753. [\[CrossRef\]](#)
13. Brown, M.; Nowotarski, C.J. The Influence of Lifting Condensation Level on Low-Level Outflow and Rotation in Simulated Supercell Thunderstorms. *J. Atmos. Sci.* **2019**, *76*, 1349–1372. [\[CrossRef\]](#)

14. Craven, J.P.; Brooks, H.E. Baseline climatology of sounding derived parameters associated with deep, moist convection. *Natl. Weather Dig.* **2004**, *28*, 13–24. Available online: https://www.nssl.noaa.gov/users/brooks/public_html/papers/cravenbrooksna.pdf (accessed on 20 March 2020).
15. Grams, J.S.; Thompson, R.L.; Snively, D.V.; Prentice, J.A.; Hodges, G.M.; Reames, L.J. A climatology and comparison of parameters for significant tornado events in the United States. *Weather Forecast.* **2012**, *27*, 106–123. [[CrossRef](#)]
16. Púčik, T.; Groenemeijer, P.; Rýva, D.; Kolář, M. Proximity soundings of severe and nonsevere thunderstorms in central Europe. *Mon. Weather Rev.* **2015**, *143*, 4805–4821. [[CrossRef](#)]
17. Taszarek, M.; Brooks, H.E.; Czernecki, B. Sounding-derived parameters associated with convective hazards in Europe. *Mon. Weather Rev.* **2017**, *145*, 1511–1528. [[CrossRef](#)]
18. Esterheld, J.M.; Giuliano, D.J. Discriminating between tornadic and non-tornadic supercells: A new hodograph technique. *E-J. Sev. Storms Meteorol.* **2008**, *3*, 2. Available online: <https://ejssm.org/ojs/index.php/ejssm/article/viewArticle/33> (accessed on 20 March 2020).
19. Nowotarski, C.J.; Jensen, A.A. Classifying proximity soundings with self-organizing maps toward improving supercell and tornado forecasting. *Weather Forecast.* **2013**, *28*, 783–801. [[CrossRef](#)]
20. Coffey, B.E.; Parker, M.D.; Dahl, J.M.; Wicker, L.J.; Clark, A.J. Volatility of tornadogenesis: An ensemble of simulated nontornadic and tornadic supercells in VORTEX2 environments. *Mon. Weather Rev.* **2017**, *145*, 4605–4625. [[CrossRef](#)]
21. Coffey, B.E.; Parker, M.D. Is there a “tipping point” between simulated nontornadic and tornadic supercells in VORTEX2 environments? *Mon. Weather Rev.* **2018**, *146*, 2667–2693. [[CrossRef](#)]
22. Coffey, B.E.; Parker, M.D.; Thompson, R.L.; Smith, B.T.; Jewell, R.E. Using near-ground storm relative helicity in supercell tornado forecasting. *Weather Forecast.* **2019**, *34*, 1417–1435. [[CrossRef](#)]
23. Kain, J.S.; Weiss, S.J.; Bright, D.R.; Baldwin, M.E.; Levit, J.J.; Carbin, G.W.; Schwartz, C.S.; Weisman, M.L.; Droegemeier, K.K.; Weber, D.B.; et al. Some practical considerations regarding horizontal resolution in the first generation of operational convection-allowing NWP. *Weather Forecast.* **2008**, *23*, 931–952. [[CrossRef](#)]
24. Seity, Y.; Lac, C.; Bouyssel, F.; Riette, S.; Bouteloup, Y. Cloud and microphysical schemes in ARPEGE and AROME models. In Proceedings of the ECMWF Workshop on Parametrization of Clouds and Precipitation, Shinfield Park, Reading, UK, 5–8 November 2012; Available online: <https://www.ecmwf.int/en/elibrary/12167-cloud-and-microphysical-schemes-arpege-and-arome-models> (accessed on 20 May 2020).
25. Brousseau, P.; Seity, Y.; Ricard, D.; Léger, J. Improvement of the forecast of convective activity from the AROME-France system. *Q. J. R. Meteorol. Soc.* **2016**, *142*, 2231–2243. [[CrossRef](#)]
26. Weisman, M.L.; Evans, C.; Bosart, L. The 8 May 2009 super-derecho: Analysis of a real-time explicit convective forecast. *Weather Forecast.* **2013**, *28*, 863–892. [[CrossRef](#)]
27. Sobash, R.A.; Kain, J.S.; Bright, D.R.; Dean, A.R.; Coniglio, M.C.; Weiss, S.J. Probabilistic forecast guidance for severe thunderstorms based on the identification of extreme phenomena in convection-allowing model forecasts. *Weather Forecast.* **2011**, *26*, 714–728. [[CrossRef](#)]
28. Clark, A.J.; Kain, J.S.; Marsh, P.T.; Correia, J., Jr.; Xue, M.; Kong, F. Forecasting tornado pathlengths using a three-dimensional object identification algorithm applied to convection-allowing forecasts. *Weather Forecast.* **2012**, *27*, 1090–1113. [[CrossRef](#)]
29. Clark, A.J.; Gao, J.; Marsh, P.T.; Smith, T.; Kain, J.S.; Correia, J.; Xue, M.; Kong, F. Tornado pathlength forecasts from 2010 to 2011 using ensemble updraft helicity. *Weather Forecast.* **2013**, *28*, 387–407. [[CrossRef](#)]
30. Sobash, R.A.; Schwartz, C.S.; Romine, G.S.; Fossell, K.R.; Weisman, M.L. Severe weather prediction using storm surrogates from an ensemble forecasting system. *Weather Forecast.* **2016**, *31*, 255–271. [[CrossRef](#)]
31. Gallo, B.T.; Clark, A.J.; Dembek, S.R. Forecasting tornadoes using convection-permitting ensembles. *Weather Forecast.* **2016**, *31*, 273–295. [[CrossRef](#)]
32. Gallo, B.T.; Clark, A.J.; Smith, B.T.; Thompson, R.L.; Jirak, I.; Dembek, S.R. Blended probabilistic tornado forecasts: Combining climatological frequencies with NSSL–WRF ensemble forecasts. *Weather Forecast.* **2018**, *33*, 443–460. [[CrossRef](#)]
33. Lawson, J.R. Predictability of idealized thunderstorms in buoyancy—Shear space. *J. Atmos. Sci.* **2019**, *76*, 2653–2672. [[CrossRef](#)]
34. Anderson-Frey, A.K.; Richardson, Y.P.; Dean, A.R.; Thompson, R.L.; Smith, B.T. Investigation of near-storm environments for tornado events and warnings. *Weather Forecast.* **2016**, *31*, 1771–1790. [[CrossRef](#)]

35. Herman, G.R.; Nielsen, E.R.; Schumacher, R.S. Probabilistic verification of Storm Prediction Center convective outlooks. *Weather Forecast.* **2018**, *33*, 161–184. [CrossRef]
36. Dotzek, N.; Groenemeijer, P.; Feuerstein, B.; Holzer, A.M. Overview of ESSL's severe convective storms research using the European Severe Weather Database ESWD. *Atmos. Res.* **2009**, *93*, 575–586. [CrossRef]
37. Smith, B.T.; Thompson, R.L.; Grams, J.S.; Broyles, C.; Brooks, H.E. Convective modes for significant severe thunderstorms in the contiguous United States. Part I: Storm classification and climatology. *Weather Forecast.* **2012**, *27*, 1114–1135. [CrossRef]
38. Šinger, M. Occurrence of supercells in Slovakia in 2000–2012. In Proceedings of the 9th European Conference of Severe Storms (ECSS), Pula, Italy, 18–22 September 2017; ECSS2017-166. Available online: https://presentations.copernicus.org/ECSS2017/ECSS2017-166_presentation.pdf (accessed on 20 May 2020).
39. Šinger, M. Tornádo in Iekárovce. *Meteorol. J.* **2018**, *21*, 109–116. Available online: http://www.shmu.sk/File/ExtraFiles/MET_CASOPIS/MC_2018-2.pdf (accessed on 28 April 2020).
40. Gerard, L.; Piriou, J.-M.; Brožková, R.; Geleyn, J.-F.; Banciu, D. Cloud and precipitation parameterization in a meso-gammascale operational weather prediction model. *Mon. Weather Rev.* **2009**, *137*, 3960–3977. [CrossRef]
41. Brožková, R.; Bučánek, A.; Mašek, J.; Smoliková, P.; Trojáková, A. Nová provozní konfigurace modelu Aladin ve vysokém rozlišení. *Meteorol. Zprávy* **2019**, *72*, 129–139. Available online: http://www.cmes.cz/sites/default/files/chmu_mz_5-19_129-139.pdf (accessed on 6 June 2020).
42. Derková, M.; Vivoda, J.; Belluš, M.; Španiel, O.; Dian, M.; Neštiak, M.; Zehnal, R. Recent improvements in the ALADIN/SHMU operational system. *Meteorol. J.* **2017**, *20*, 45–52. Available online: http://www.shmu.sk/File/ExtraFiles/MET_CASOPIS/2017-2_MC.pdf (accessed on 28 April 2020).
43. Termonia, P.; Fischer, C.; Bazile, E.; Bouyssel, F.; Brožková, R.; Bénard, P.; Bochenek, B.; Degrauwe, D.; Derková, M.; El Khatib, R.; et al. The ALADIN System and its Canonical Model Configurations AROME CY41T1 and ALARO CY40T1. *Geosci. Model Dev.* **2018**, *11*, 257–281. [CrossRef]
44. Lopez, P. Implementation and validation of a new prognostic large-scale cloud and precipitation scheme for climate and data assimilation purposes. *Q. J. R. Meteorol. Soc.* **2002**, *128*, 229–257. [CrossRef]
45. Jurásek, M.; Kaňák, J.; Okon, L.; Méri, L. Calibration & monitoring of Slovak weather radar network. In Proceedings of the Weather Radar Calibration & Monitoring Workshop, 18–20 October 2017; Available online: https://www.dwd.de/EN/specialusers/research_education/met_applications_specials/wxrcalmon2017_presentations/poster_downloads/16_jurasek_wxrcalmon2017_poster.pdf?__blob=publicationFile&v=2 (accessed on 6 June 2020).
46. Thompson, R.L.; Smith, B.T.; Grams, J.S.; Dean, A.R.; Broyles, C. Convective modes for significant severe thunderstorms in the contiguous United States. Part II: Supercell and QLCS tornado environments. *Weather Forecast.* **2012**, *27*, 1136–1154. [CrossRef]
47. Bunkers, M.J.; Klimowski, B.A.; Zeitler, J.W.; Thompson, R.L.; Weisman, M.L. Predicting supercell motion using a new hodograph technique. *Weather Forecast.* **2000**, *15*, 61–79. [CrossRef]
48. Anderson-Frey, A.K.; Richardson, Y.P.; Dean, A.R.; Thompson, R.L.; Smith, B.T. Near-storm environments of outbreak and isolated tornadoes. *Weather Forecast.* **2018**, *33*, 1397–1412. [CrossRef]
49. Grünwald, S.; Brooks, H.E. Relationship between sounding derived parameters and the strength of tornadoes in Europe and the USA from reanalysis data. *Atmos. Res.* **2011**, *100*, 479–488. [CrossRef]
50. Réthly, A. Időjárási események és elemi csapások Magyarországon 1801–1900-ig. *Bp. Országos Meteorológiai Szolgálat* **1998**, *1*, 226–227.
51. Živelné Pohromy na Slovensku—Tornádo v obci Slovenská Ves. Available online: <https://terabis.webgarden.cz/rubriky/zivelne-pohromy-na-slovensku/tornado-slovenska-ves> (accessed on 15 April 2020).
52. Simon, A.; Sokol, A. Tornáda a Iné Nebezpečné Búrkové Javy na Území Slovenska, Slovak Hydrometeorological Institute Report. Available online: <http://www.shmu.sk/File/studijne%20materialy/tornada.pdf> (accessed on 15 April 2020).
53. Sokol, A. Possible Tornado Occurrence in BUDATINSKA Lehota Village on 19th March 2001. 2002. Available online: <https://www.essl.org/ECSS/2002/abstracts/30.htm> (accessed on 28 April 2020).
54. Bosart, L.F.; Seimon, A.; LaPenta, K.D.; Dickinson, M.J. Supercell tornadogenesis over complex terrain: The Great Barrington, Massachusetts, tornado on 29 May 1995. *Weather Forecast.* **2006**, *21*, 897–922. [CrossRef]
55. Peyraud, L. Analysis of the 18 July 2005 tornadic supercell over the Lake Geneva region. *Weather Forecast.* **2013**, *28*, 1524–1551. [CrossRef]

56. Tang, B.; Vaughan, M.; Lazear, R.; Corbosiero, K.; Bosart, L.; Wasula, T.; Lee, I.; Lipton, K. Topographic and boundary influences on the 22 May 2014 Duaneburg, New York, tornadic supercell. *Weather Forecast.* **2016**, *31*, 107–127. [[CrossRef](#)]
57. Lyza, A.W.; Knupp, K.R. A background investigation of tornado activity across the southern Cumberland Plateau terrain system of northeastern Alabama. *Mon. Weather Rev.* **2018**, *146*, 4261–4278. [[CrossRef](#)]
58. Lyza, A.W.; Murphy, T.A.; Goudeau, B.T.; Pangle, P.T.; Knupp, K.R.; Wade, R.A. Observed Near-storm Environment Variations across the Southern Cumberland Plateau System in Northeastern Alabama. *Mon. Weather Rev.* **2020**, *148*, 1465–1482. [[CrossRef](#)]
59. Pilgaj, N.; Taszarek, M.; Pajurek, Ł.; Kryza, M. High-resolution simulation of an isolated tornadic supercell in Poland on 20 June 2016. *Atmos. Res.* **2019**, *218*, 145–159. [[CrossRef](#)]



© 2020 by the authors. Licensee MDPI, Basel, Switzerland. This article is an open access article distributed under the terms and conditions of the Creative Commons Attribution (CC BY) license (<http://creativecommons.org/licenses/by/4.0/>).